metals

MDPI

Article

Experimental and Simulation Analysis of Effects of Laser Bending on Microstructures Applied to Advanced Metallic Alloys

Esteban Ramos-Moore [1,2,*], Joaquín Hoffmann [3], Rafael H. M. Siqueira [4], Sheila Medeiros de Carvalho [4], Milton S. Fernandes de Lima [4] and Diego J. Celentano [2,3]

1 Instituto de Física, Pontificia Universidad Católica de Chile, Vicuña Mackenna 4860, Macul, Santiago 7820436, Chile
2 Centro de Investigación en Nanotecnología y Materiales Avanzados (CIEN-UC), Pontificia Universidad Católica de Chile, Vicuña Mackenna 4860, Macul, Santiago 7820436, Chile; dcelentano@ing.puc.cl
3 Departamento de Ingeniería Mecánica y Metalúrgica, Pontificia Universidad Católica de Chile, Vicuña Mackenna 4860, Macul, Santiago 7820436, Chile; jhoffmann@uc.cl
4 Photonics Division, Instituto de Estudos Avançados, São José dos Campos 12228-001, SP, Brazil; rafaelhmota@yahoo.com.br (R.H.M.S.); sheila.m.carvalho@ufes.br (S.M.d.C.); milton@ieav.cta.br (M.S.F.d.L.)
* Correspondence: evramos@uc.cl

Abstract: The aim of this work is the analysis of laser beam forming (LBF) in the bending of two relevant materials used in the transportation industry—interstitial-free (IF) steel and AA6013 high-strength aluminum alloy. Our experiments and numerical simulations consider two different operating scenarios achieved by varying the laser beam scanning velocity using linear paths. The material behavior during this process is described via a coupled thermomechanical-plasticity-based formulation that allows prediction of temperature profiles and bending angles. Metallography, glow discharge optical emission spectroscopy, and X-ray diffraction are used for microstructure characterization. In addition, microstress analyses are performed in order to study the stress behavior of the irradiated zones. It is found that LBF mainly induces grain growth and melting in the case of high surface temperatures. Before melting, the materials developed compressive stresses that could be useful in preventing cracking failures. The resulting bending angles are predicted and experimentally validated, indicating the robustness of the model to estimate LBF effects on advanced alloys. The present analysis relating bending angles together with temperature and microstructure profiles along the thickness of the sheets is the main original contribution of this work, highlighting the need for further modeling refinement of the effects of LBF on advanced alloys to include more microstructural properties, such as grain boundary diffusion and surface roughness.

Keywords: laser beam forming; microstructure; interstitial-free steels; aluminum alloys; modeling and numerical simulation

Citation: Ramos-Moore, E.; Hoffmann, J.; Siqueira, R.H.M.; Medeiros de Carvalho, S.; Fernandes de Lima, M.S.; Celentano, D.J. Experimental and Simulation Analysis of Effects of Laser Bending on Microstructures Applied to Advanced Metallic Alloys. *Metals* **2021**, *11*, 362. https://doi.org/10.3390/met11020362

Academic Editor: Gleb A. Turichin

Received: 27 January 2021
Accepted: 16 February 2021
Published: 21 February 2021

1. Introduction

Laser beam forming (LBF) is a contactless process for sheet bending of ductile metals, in which a laser beam heats specific zones of a material, generating thermal stresses that exceed its yield strength and inducing plastic deformation that finally bends the metallic sheet [1]. Recently, research carried out on LBF for bending has mainly focused on the thermomechanical effects of operating variables, such as the laser beam diameter, power and velocity, surface coating, and sheet dimensions [2–6]. In parallel, other authors have developed scanning strategies to manufacture parts of complex geometries, such as single and multi-run sequences and linear and curved laser paths [3,7–12]. Thus, this kind of forming method has recently become a viable and widespread process to be applied in shaping different metallic components, especially due to the sophistication of laser techniques and their wide availability in various industries.

A wide range of metallic materials have been treated via LBF for bending and welding purposes, e.g., AISI 1010 [5,7,13–15] and S275 [8] mild steels, AISI 302 [11,16] and AISI 304 [4,6,11,12,17] stainless steels, AA 6013 aluminum alloy under both annealed and as-welded conditions [18,19], AA 2024-T3 aluminum alloy, and Ti6Al4V titanium alloy [3]. In addition, the influence of material properties on the LBF process has been addressed via numerical simulations in terms of the relationship between the final bending angle and material parameters, such as the Young's modulus, yield strength, thermal expansion coefficient, specific heat, and thermal conductivity [20]. Despite the progress made in this field, there are still some aspects that require further investigation, such as the resulting microstructures obtained for materials processed via LBF under different operating conditions. This subject is particularly relevant in many specific applications that usually require control over the integrity of the material after the forming process, e.g., in aerospace, microelectronics, and automotive industries.

The aim of this work is to assess the performance of multi-run LBF for bending applied to two relevant materials used in the transportation industry: interstitial-free (IF) steel and AA6013 aeronautical aluminum alloy. To this end, LBF experiments were first carried out using two laser beam scanning velocities with five overlapping linear paths. The characterization of the final microstructure through thickness profiles obtained in these scenarios was performed via metallography, glow discharge optical emission spectroscopy (GDOES), and X-ray diffraction (XRD). The stresses developed in the bending area were estimated on the basis of XRD peak shifts. The bending angle evolution was experimentally obtained by measuring the height at the edge of the sample with the use of a dedicated dial gauge. Then, numerical simulations were performed to predict thermal profiles within the metal sheet during the LBF process using a coupled thermomechanical-plasticity-based formulation accounting for large strains, temperature-dependent material properties, and convection–radiation phenomena. The full formulation was discretized and solved in the context of the finite element method (FEM). From the obtained experimental and numerical results, correlation maps between the energy input, resulting microstructure, and the final bending angle were established. As a preliminary experimental validation of the numerical predictions, the proposed methodology was initially applied to the AISI 304 stainless steel, since this material has been extensively used in LBF operations, and therefore was adopted in the present study as a reference material. Finally, the obtained results relating the bending angle together with temperature and microstructure profiles along the thickness of the sheet not only constitute the main original contribution of this work, but also highlight the use of novel modeling approaches for laser beam forming treatments on advanced metallic alloys.

2. Materials and Methods

2.1. Materials

The materials analyzed in this study are IF steel and AA 6013 aluminum alloy. AISI 304 stainless steel is also considered as a reference material due to the large number of studies available on this material; therefore, it is considered in the present work to validate the proposed experimental numerical analysis methodology. These materials were provided in sheets measuring 1.0, 0.7 and 1.6 mm thickness for the AISI 304 steel, IF steel, and AA 6013 aluminum, respectively. The IF steel was provided in as-annealed state and AA 6013 in T4 (naturally aged) condition.

2.2. Laser Bending Experiment

The bending experiment was carried out with a moving laser beam on sheet samples measuring 76 mm long and 60 mm wide. The scanning path was along the full width of the sample at approximately the middle of its length and always perpendicular to the sheet rolling direction. Five runs along this path were considered, with a time interval between runs of 5 s. The sample was firmly clamped on one edge and free to move at the other edge. The experiments were carried out with a model YLR-2000 Yb-fiber laser (IPG Photonics

Corp., Oxford, MA, USA) from IPG Pho-tonics, with a maximum power of 2 kW. The main laser parameters for the LBF treatment are shown in Table 1. The laser head was positioned above the focal plane to achieve an effective bean diameter of 2 mm at the surface of each sample. In all cases, a graphite layer was applied to improve absorptivity, resulting in an absorption coefficient of approximately 0.7 [21].

Table 1. The main laser parameters of the LBF treatment. The final linear energy refers to the accumulated energy after five runs (AISI 304 stainless steel, interstitial-free (IF) steel and AA6013 aluminum alloy).

Sample	Laser Power (W)	Scanning Velocity (mm/s)	Linear Energy (J/mm)	Final Linear Energy (J/mm)
AISI 304	100	10	10	50
		5	20	100
IF Steel	100	10	10	50
		5	20	100
AA 6013	200	10	20	100
		5	40	200

2.3. Numerical Simulation

A numerical simulation of the material response during the LBF process was performed with a previously reported coupled thermomechanical-plasticity-based formulation [17,18,22], which accounts for large strains, temperature-dependent material properties, and convection–radiation phenomena. This model is solved in the context of FEM using a 3D mesh composed of nearly 19,000 eight-node elements using an in-house code. A discretization refinement was considered along the laser scanning path in order to adequately capture the steep gradients in the thermomechanical variables caused by the localized heat flux provided by the laser beam. The selected time step was 0.01 s and the temperature-dependent thermomechanical properties of the three studied materials were taken from the literature [17,18,22]. This model allows the prediction of bending angles and temperature profiles along the thickness of the samples at the laser beam path. Potential phase transformations are, for simplicity, precluded in the modeling.

2.4. Microstructure Characterization

Samples before and after the LBF treatment were cut and set for metallographic analysis trough grinding with silicon carbide sandpaper, polished with alumina, and chemically attacked according to the ASTM E407-07 standard using a Nikon Optiphot microscope (Nikon Corp., Tokio, Japan). The images in the case of the AISI 304 sample were post-processed with ImageJ software (U.S. National Institutes of Health, Bethesda, MD, USA) to quantify the area of observed pearlite grains.

Glow discharge optical emission spectroscopy (GDOES, Spectruma Analytik GmbH, Hof, Germany) was carried out using a glow discharge analyzer (GDA) 750 HR instrument from Spectruma Analytik GmbH to study the elemental composition of the samples. Throughout the bulk profile analysis, the elemental composition of the samples was quantified within the first micrometers in depth. The measurements were performed with a 2.5 mm diameter anode and operating in DC excitation mode. Every sample was measured twice, and the glow was obtained in argon atmosphere (5.0 quality) at an average discharge pressure of 5×10^{-2} hPa. The excitation parameters of the measurements were 1000 eV and 12 mA and the sputtering rate was calculated so that the measuring depth was around 3 µm. Quantified profiles of atomic concentration vs. depth were obtained automatically using the standard WinGDOES software (Spectruma Analytik GmbH, Hof, Germany).

To assess the identification and quantification of the main phases, 2θ scans with a 0.02° step size and seven seconds dwell time per step were carried out in a Bruker D8 Advance X-ray diffractometer (Bruker Corp., Billerica, MA, USA). A CuKα source was used, with a 40 kV accelerating voltage and 40 mA filament current. Gaussian multi-peak curve fitting

was carried out in order to estimate the parameters of the reflection peaks, such as the position and intensity [23]. The data obtained was compared with known phases of the corresponding materials available in the Cristal Open Database [24].

2.5. Stress Analysis

The stresses produced by the different treatments were estimated on the basis of the relative variations of the peak positions after the LBF treatment. Although residual stresses might be present before the treatments, the peak positions of the non-treated samples are assumed as the reference zero-stress angles. To determine the elastic stresses, Hooke's law is applied using the Reuss method [25], which allows one to calculate the Young's moduli as a function of the crystal orientation.

3. Results and Analysis

3.1. Laser Bending

The resulting sheets after the LBF treatment for bending are shown in Figure 1. The final bending angle was estimated by trigonometry after measuring the vertical displacement of the free end of the sample (h) and the horizontal distance of the bent plate (a), as indicated in Figure 1B. The bending angles obtained were 9.8° (10 mm/s) and 13.3° (5 mm/s) for AISI 304 steel, 11.1° (10 mm/s) and 15.2° (5 mm/s) for IF steel, and 6.8° (10 mm/s) and 7.6° (5 mm/s) for AA 6013 aluminum alloy.

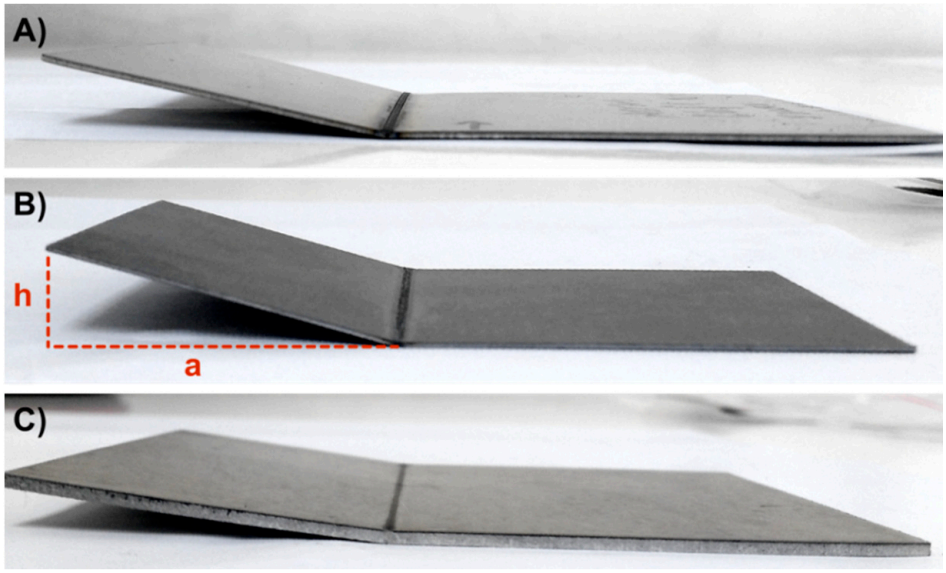

Figure 1. Resulting sheets after the LBF treatment for bending: (**A**) AISI 304 stainless steel, (**B**) interstitial free (IF) steel, and (**C**) AA 6013 aluminum alloy samples subjected to LBF. The parameters a and h were used to calculate the bending angle for the different cases.

The simulated bending angle at the end of each laser run and the experimental angle at the end of the LBF process, after five runs, are shown in Figure 2. The experimental final bending angle agrees with the numerical simulation for the three analyzed materials. Moreover, the results of the models for the three materials show that the number of laser beam runs promotes larger bending angles, with a roughly linear relationship between the bending angle and number of irradiations for the scanning velocity of 10 mm/s and higher rates after each run for the scanning velocity of 5 mm/s.

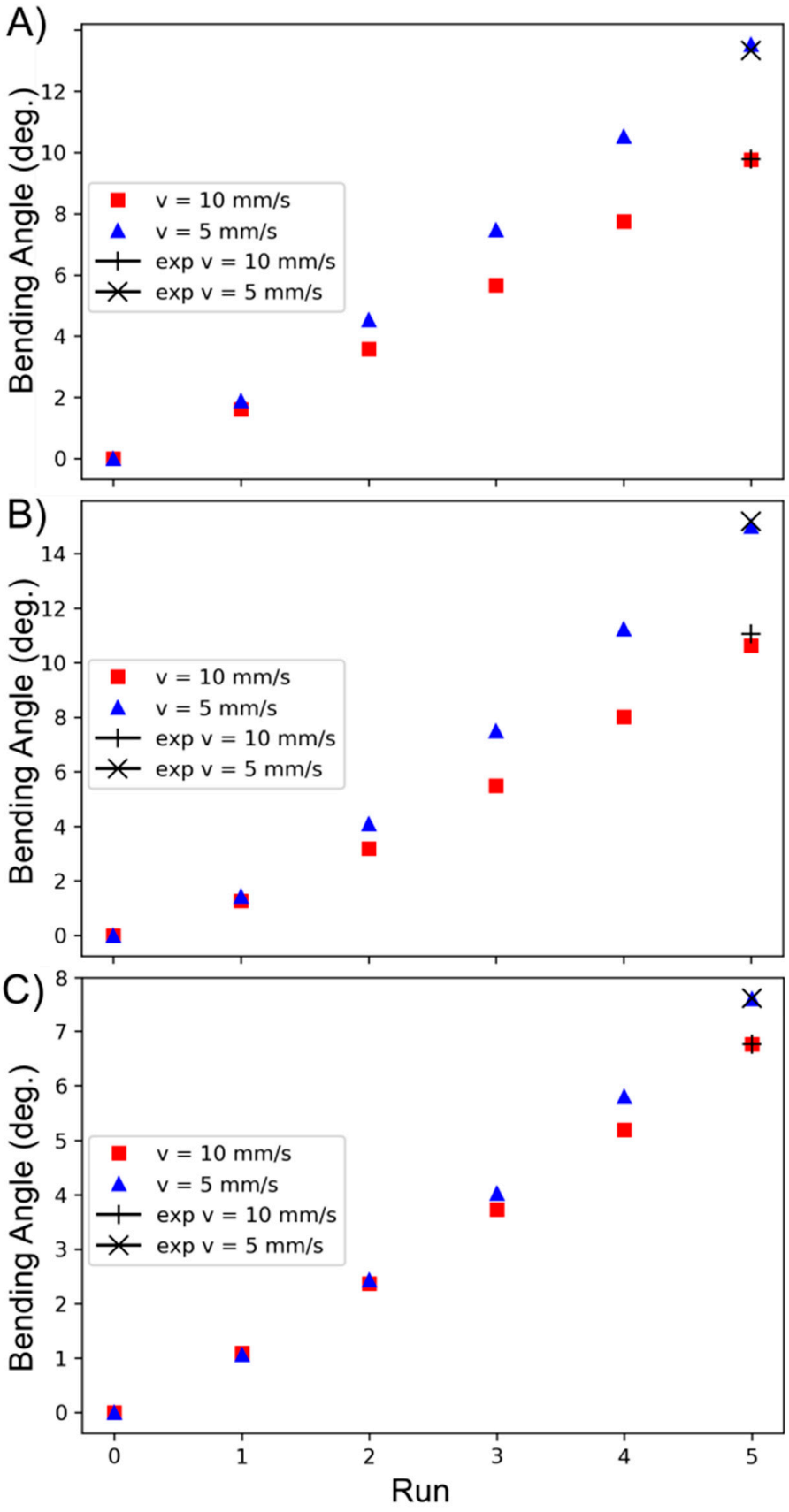

Figure 2. Experimental (exp) and simulated bending angles in degrees (deg.) for (**A**) AISI 304 steel, (**B**) IF steel and (**C**) AA 6013 aluminum samples subjected to LBF.

3.2. Microstructure

In terms of chemical composition, AISI 304 alloy contains austenite at room temperature thanks to the addition of Cr and Ni [13]. IF steels have low carbon contents and are mainly made up of ferrite, which is a soft phase that facilitates their machinability. Greater proportions of carbon imply harder constituents, such as pearlite [14]. AA 6013 alloy is corrosion-resistant and is strengthened by precipitation, mainly using Mg_2Si and Cu [5]. Table 2 shows the compositions in wt.% of the non-treated materials measured by GDOES and of the standard materials. The AISI304 sample agrees with the standard from Unified National Special (UNS), but with 3% less Cr and 1.1% more Mg. The IF steel shows more C than the standard and can be classified as a low-carbon steel (<0.1% wt.). The AA6013 sample agrees with the standard but with 0.1% less Si. These deviations are within the range of frequent errors and can be tracked to concentration inhomogeneities due to fabrication or measurement procedures.

Table 2. Compositions in wt.% of the non-treated materials measured by GDOES and of the standard materials (AISI 304 stainless steel, interstitial-free (IF) steel and AA6013 aluminum alloy).

Material	Source	Fe	Al	Mn	C	Ni	Cr	Cu	Si	P	Mg
AISI 304	This work	Bal.	-	3.1	0.03	8.6	15	0.4	0.4	0.3	-
	UNS S30400	-	-	≤2	≤0.08	8–10.5	18–20	-	≤1	≤0.045	-
IF Steel	This work	Bal.	0.07	0.14	0.04	0.03	0.01	0.01	-	-	-
	VDA 239-100	Bal	≥0.01	≤1.6	≤0.01	-	-	≤0.2	≤0.3	≤0.1	-
AA 6013	This work	0.3	Bal.	0.4	-	-	-	0.8	0.5	-	0.8
	UNS A96013	≤0.5	Bal.	0.2–0.8	-	-	≤0.1	0.6–1.1	0.6–1	-	0.8–1.2

The effect of the LBF treatment on the microstructures of the samples is shown in Figure 3. Both metallography images and simulated temperature profiles (blue lines) are included. The simulated data predict the temperatures directly below the center point of the laser path as a function of depth. Red lines indicate the affected zones where the microstructures changed due to the laser radiation, which is characterized by a Gaussian distribution of energy. Two relevant positions are analyzed—the surfaces and front points (deepest point) of the affected zones. These data are shown and compared with the solidus–liquidus temperatures of samples in Table 3.

For all samples, as expected, the front point temperatures were lower than surface temperatures and higher for 5 than 10 mm/s measurements. When decreasing the scanning speed from 10 to 5 mm/s, i.e., increasing the interaction time, and therefore the amount of absorbed energy, the front point depth increased by 90% for steels and by 20% for aluminum. This difference can mainly be explained by differences in the thermal diffusivity of each material, being higher in aluminum than in steel.

Table 3. Surface and front point temperatures of the affected zones (red line) shown in Figure 3 and standard melting temperatures.

Material	Front-Point Depth (μm)		Front-Point Temperature (°C)		Surface Temperature (°C)		Melting Temperature (°C)
Scanning Velocity	10 mm/s	5 mm/s	10 mm/s	5 mm/s	10 mm/s	5 mm/s	Solidus–Liquidus
AISI 304	82	153	1075	1158	1270	1465	1400–1450
IF Steel	121	224	1047	1275	1232	1520	~1540
AA 6013	245	285	385	473	530	611	580–650

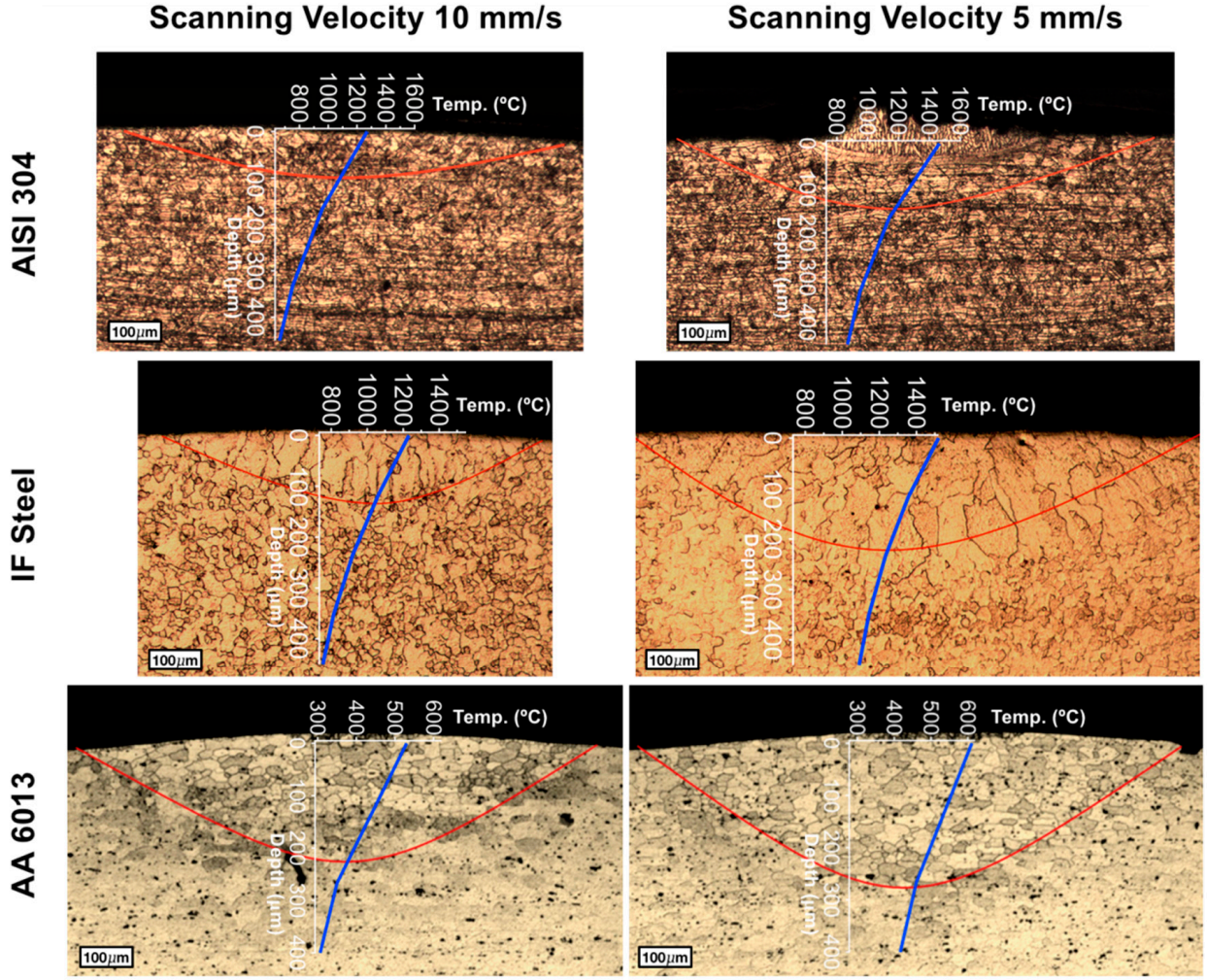

Figure 3. Metallography images and simulated temperature profiles (blue lines) along the sample depth at the middle point of the laser path for samples subjected to LBF. Red lines indicate the affected zones where microstructure changed due to the laser radiation. The deepest affected zone is called the front point zone.

XRD diffractograms of the treated samples and the corresponding phases are shown in Figure 4. The samples were analyzed directly on the laser path zones (see Figure 1), and therefore the diffractograms are representative of the affected zones shown in Figure 3. Non-treated and laser-scanned samples treated for 5 and 10 mm/s are shown. For AISI 304, the main phases are γ-iron (PDF 00-023-0298) and iron–nickel (PDF 00-039-0246). For IF steel, the main phases are α-iron (PDF 00-006-0696), wuestite $Fe_{2.959}O_4$ (PDF 01-086-1347), and magnetite $Fe_{3.57}O_4$ (PDF 96-101-1164). For AA 6013, the main phases are Al (PDF 01-085-1327) and Fe-Cr (PDF 00-039-0246). It is worth noting that no significant changes were observed in the diffractograms after the laser treatment, except for the IF steel scanned with a laser velocity of 5 mm/s, which showed higher intensity peaks of iron oxides. This fact can be tracked to the high temperatures produced by the LBF treatment, as shown by our simulated temperature profiles (see Figure 3) and in agreement with the results from Sinha et al. [26].

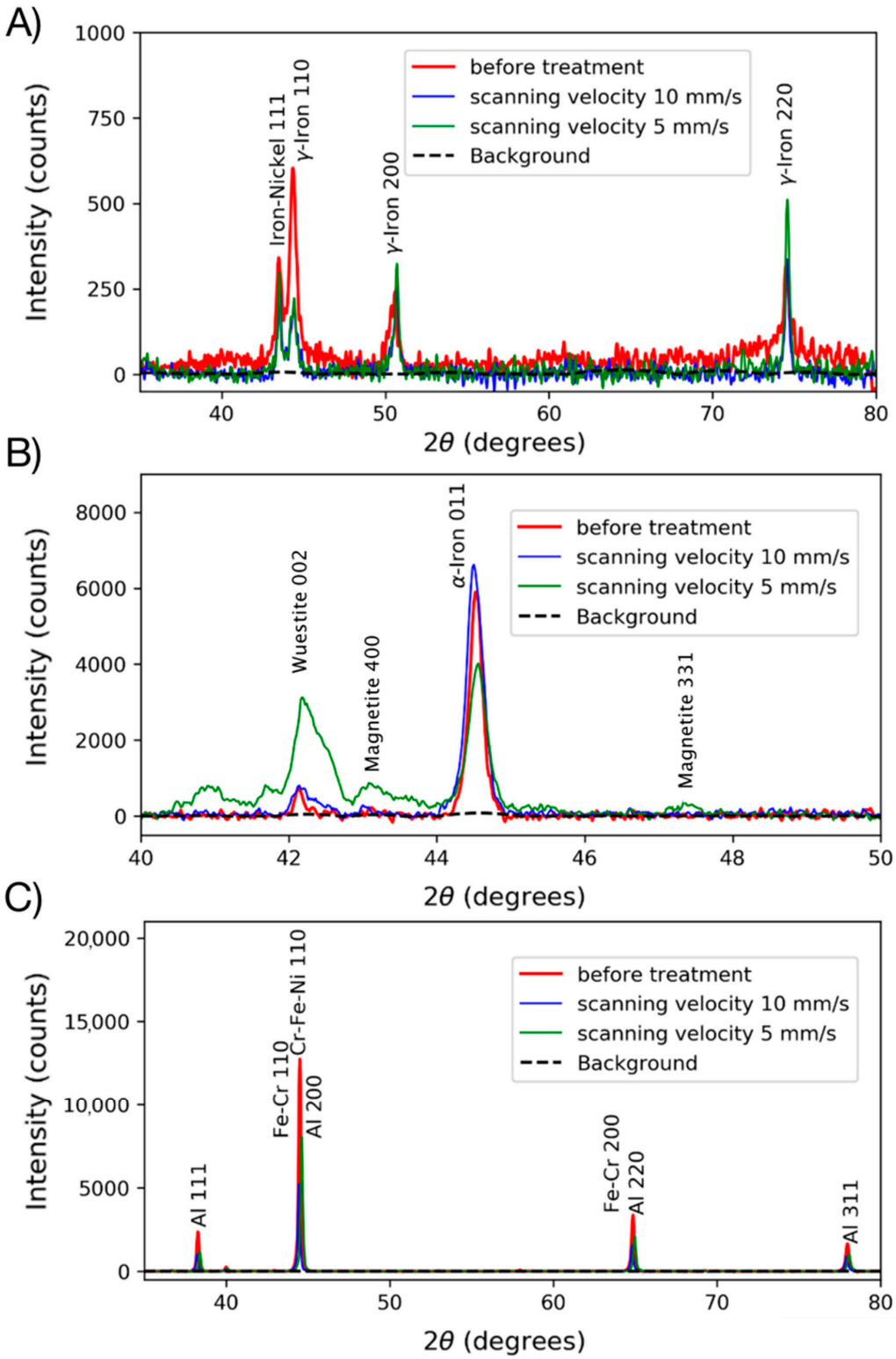

Figure 4. X-ray diffraction (XRD) diffractograms of the samples showing the main reflections of the phases for (**A**) AISI 304 steel, (**B**) IF steel, and (**C**) AA 6013 aluminum samples subjected to LBF.

3.3. Stress Analysis

In order to deeply analyze the behavior of the matrix phases after the laser treatment, Figure 5 shows magnified views of the XRD diffractograms of the selected phases, showing the peak shifts in the different samples subjected to LBF. It is worth noting that for all samples and scanning velocities, both the peak intensity and angle position changed.

The former can be attributed to grain growth and the latter to the presence of residual stresses [27,28]. In this regard, the peaks shown in Figure 5 were adjusted with Gaussian profiles in order to quantify the peak shifts, and thereafter the stress development relative to the non-treated sample. Due to their isolation (non-convolution), the following reflection peaks were chosen for stress analysis: 110 of γ-iron for AISI 304, 001 of α-iron for IF steel, and 311 of Al for AA 6013.

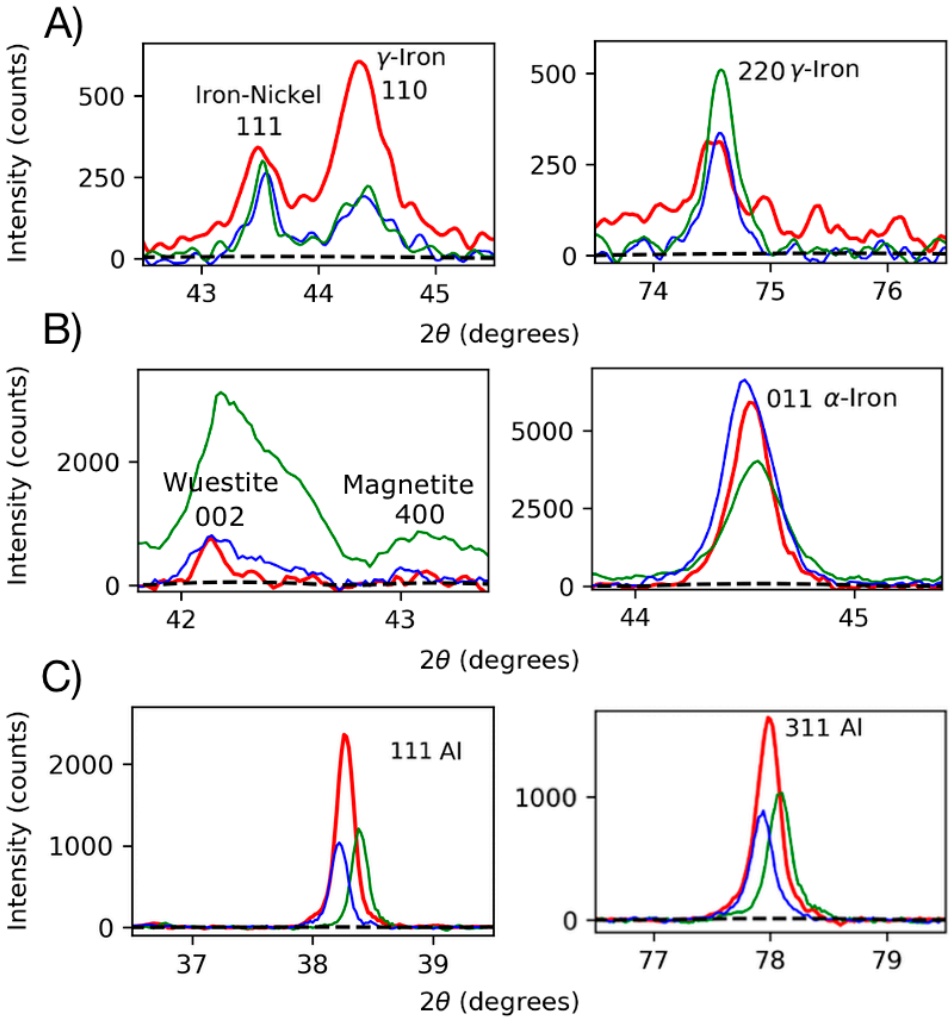

Figure 5. Magnified views of the XRD diffractograms of the selected phases showing the shifts in the different reflection peaks for (**A**) AISI 304 steel, (**B**) IF steel, and (**C**) AA6013 aluminum samples subjected to LBF. Red line: before treatment; blue line: scanning velocity of 10 mm/s; green line: scanning velocity of 5 mm/s; dashed line: background.

The elastic stresses (σ) developed in the bending area were estimated on the basis of XRD peak shifts using Hooke's law and the Reuss model. The former correlates the deformation of the interatomic spacing with the stress through Young's modulus, while the latter assumes constant stress in all grains of the polycrystal. The values estimated in the metal matrices of samples AISI 304, IF and AA 6013 subjected to LBF with two different scanning velocities are shown in Table 4. These stresses were estimated with respect to the initial state of the samples, i.e., before the LBF treatment, and therefore cannot be interpreted as residual stresses. As a direct observation, all of the matrices changed their stress state depending on the scanning velocity. When decreasing the scanning velocity from 10 to 5 mm/s, AISI 304 changed from compression to high tension (0.5 GPa), whereas IF steel and AA 3016 changed from tension to compression, being almost zero (−5 MPa) in the case of IF steel. It is worth noting that these stresses are representative of a local volume

in the micro range, and do not represent the macro stress of the sheet, which indeed is responsible for the bending direction.

Table 4. Elastic stresses (σ) estimated in the metal matrices of samples AISI 304, IF, and AA 6013 subjected to LBF with two different scanning velocities.

Treatment Condition	Elastic Stresses (σ)	
	AISI 304	
Scanning Velocity σ(110 γ-Iron)	10 mm/s −90 MPa	5 mm/s 527 MPa
	IF	
Scanning Velocity σ(011 α-Iron)	10 mm/s 190 MPa	5 mm/s −5 MPa
	AA 6013	
Scanning Velocity σ(311 Al)	10 mm/s 42 MPa	5 mm/s −63 MPa

4. Discussion

The bending angles found in this work (see Figure 2) agree with experimental and simulations results found in the literature for AISI 304 [3,12,17,21] when comparing treatments with similar linear energy. To the best of our knowledge, no work has reported bending angle values for IF steel sheets, whereas few experimental results have been published for AA 6013 aluminum [18], which agree with our values. Moreover, our results show that the increment in the bending angle when decreasing the scanning speed, i.e., increasing the interaction time, and therefore the absorbed energy, is 36% for both steels and 12% for aluminum. This fact suggests that the absorption of energy is more dependent on the material's matrix than surface properties such as roughness and topography. In order to prove this hypothesis, further development of the model must include such properties.

The temperatures simulated in the affected zone for the scanning velocity of 5 mm/s are close to the solidus–liquidus temperatures, and therefore the natural question arises: why there is no strong evidence of melting in the metallography images (see Figure 3)? To answer this question, a balance of energy must be analyzed. The model takes into account the absorption of energy to increase the temperature (specific heat) and to the phase transition (latent heat), but not the energy that is absorbed for grain growth processes. As shown in the metallography images, grain growth is evident for all the samples and for all scanning speeds of the LBF treatment. Indeed, the activation energy for the grain boundary diffusion is about 84 kJ/mol for Al, whereas it is 174 kJ/mol for Fe [29], which explains the higher observed front point depth, i.e., the higher amount of grain that grows, in aluminum over steels (see Figure 2). In this regard, further studies will be devoted to the incorporation of grain border diffusion into the current model and to better quantify the grain growth process through electron backscattered diffraction (EBSD), as performed by Suarez et al. [28].

By definition, LBF processes are achieved by introducing thermal stresses into the material with a laser beam, which consequently develops macrostresses without melting. In our case, the stresses estimated by XRD correspond to microstresses due to local effects produced by the LBF treatment only, i.e., no residual stresses, and therefore the correlation with the bending angle is not straightforward. Nevertheless, the estimated microstresses can be correlated with the microstructure observed in the heat-affected zones (see Figure 3). When energy is absorbed by the substrate, both heating and grain growth processes take place, inducing local expansion of the affected zone within the matrix. Therefore, the more energy absorbed in the case of lower scanning velocity, the greater the compressive state of the affected zone. This is the behavior observed for IF and AA 6013 samples, changing from tensile to compressive stresses when decreasing the scanning speed. Compressive stresses at the surface are useful for preventing tensional states that end in cracking failures. For AISI 304, the opposite behavior is observed, changing from compressive to tensile stresses

when decreasing the scanning speed. This fact can be tracked to the surface melting shown in the metallographic image for the 5 mm/s sample (see Figure 3), which corresponds to a process that releases bulk stresses.

5. Conclusions

An analysis of LBF for bending applied to two relevant materials used in the transportation industry has been presented. The present analysis relating bending angles together with temperature and microstructure profiles along the thickness of a sheet is the main original contribution of this work. Considering the literature review, as well as the microstructural data on the effects of the LBF treatment, the following main conclusions can be stated:

- Bending angles due to the treatment were predicted and experimentally validated, and therefore the model can be applied to other advanced alloys;
- The treatment mainly induces grain growth and melting in the case of high surface temperatures;
- Before melting, the materials develop compressive microstresses that prevent cracking failure;
- Further modeling must include more microstructure effects, such as grain border diffusion and surface roughness.

Author Contributions: E.R.-M. and S.M.d.C. proposed the methodology and results analyses followed in this research, J.H., R.H.M.S. and M.S.F.d.L. carried out the experimental tests, D.J.C. performed the numerical simulations and all authors participated in the discussion of results and writing of the manuscript. All authors have read and agreed to the published version of the manuscript.

Funding: The authors thank the financial support provided by the National Agency of Research and Development (ANID)-Chile through projects FONDEQUIP EQM160091 and FONDECYT 1180591 and 1180564.

Data Availability Statement: Any requirement about the data of this research must be consulted directly to the corresponding author.

Acknowledgments: The authors thank the contribution of Néstor Catalán for XRD data analysis.

Conflicts of Interest: The authors declare no conflict of interest.

References

1. Magee, J.; Watkins, K.G.; Steen, W.M. Advances in laser forming. *J. Laser Appl.* **1998**, *10*, 235. [CrossRef]
2. Maji, K.; Shukla, R.; Nath, A.; Pratihar, D. Finite Element Analysis and Experimental Investigations on Laser Bending of AISI304 Stainless Steel Sheet. *Procedia Eng.* **2013**, *64*, 528–535. [CrossRef]
3. Navarrete, Á.; Cook, F.; Celentano, D.; Cruchaga, M.; García-Herrera, C. Numerical Simulation and Experimental Validation of Sheet Laser Forming Processes Using General Scanning Paths. *Materials* **2018**, *11*, 1262. [CrossRef]
4. Cook, F.; Miró, L.; Celentano, D.; Ramos-Grez, J. Effect of inclination angle on the absorptance of a graphite-coated cold-rolled steel sheet irradiated by laser. *J. Laser Appl.* **2016**, *28*, 022001. [CrossRef]
5. Safari, M.; Farzin, M.; Ghaei, A. Investigation into the effects of process parameters on bending angle in the laser bending of tailor machined blanks based on a statistical analysis. *J. Laser Appl.* **2013**, *25*, 052001. [CrossRef]
6. Shen, H.; Vollertsen, F. Modelling of laser forming—An review. *Comput. Mater. Sci.* **2009**, *46*, 834–840. [CrossRef]
7. Watkins, K.G.; Edwardson, S.P.; Magee, J.; Dearden, G.; French, P.; Cooke, R.L.; Sidhu, J.; Calder, N.J. *Laser Forming of Aerospace Alloys*; SAE Technical Paper; SAE International: Warrendale, PA, USA, 2001. [CrossRef]
8. Safari, M.; Farzin, M. Experimental investigation of laser forming of a saddle shape with spiral irradiating scheme. *Opt. Laser Technol.* **2015**, *66*, 146–150. [CrossRef]
9. Chakraborty, S.S.; More, H.; Nath, A.K. Laser forming of a bowl shaped surface with a stationary laser beam. *Opt. Lasers Eng.* **2016**, *77*, 126–136. [CrossRef]
10. Cook, F.; Celentano, D.; Ramos-Grez, J. Experimental-numerical methodology for the manufacturing of cranial prosthesis via laser forming. *Int. J. Adv. Manuf. Technol.* **2016**, *86*, 2187–2196. [CrossRef]
11. Tavakoli, A.; Naeini, H.M.; Roohi, A.H.; Gollo, M.H.; Shahabad, S.I. Codification of scan path parameters and development of perimeter scan strategies for 3D bowl-shaped laser forming. *Opt. Laser Technol.* **2018**, *98*, 121–133. [CrossRef]
12. Navarrete, Á.; Celentano, D. Effect of workpiece geometry using circular scan patterns in sheet laser forming processes. *Int. J. Adv. Manuf. Technol.* **2018**, *96*, 1835–1846. [CrossRef]

13. Gollo, M.H.; Mahdavian, S.; Naeini, H.M. Statistical analysis of parameter effects on bending angle in laser forming process by pulsed Nd:YAG laser. *Opt. Laser Technol.* **2011**, *43*, 475–482. [CrossRef]
14. Safari, M. Numerical Investigation of the Effect of Process and Sheet Parameters on Bending Angle in the Laser Bending Process. *World J. Mech.* **2014**, *4*, 97–101. [CrossRef]
15. Gautam, S.; Singh, S.; Dixit, U. Laser Forming of Mild Steel Sheets Using Different Surface Coatings. In *Lasers Based Manufacturing*; Springer: New Delhi, Indian, 2015; pp. 17–39. ISBN 978-81-322-2351-1.
16. Stevens, V.; Celentano, D.; Ramos-Grez, J.; Walczak, M. Experimental and Numerical Analysis of Low Output Power Laser Bending of Thin Steel Sheets. *J. Manuf. Sci. Eng.* **2012**, *134*, 031010. [CrossRef]
17. Castillo, J.I.; Celentano, D.J.; Cruchaga, M.A.; García-Herrera, C.M. Characterization of strain rate effects in sheet laser forming. *Comptes Rendus Mécanique* **2018**, *346*, 794–805. [CrossRef]
18. Siqueira, R.H.M.; Carvalho, S.M.; Kam, I.K.L.; Riva, R.; Lima, M.S.F. Non-contact sheet forming using lasers applied to a high strength aluminum alloy. *J. Mater. Res. Technol.* **2016**, *5*, 275–281. [CrossRef]
19. Costanza, G.; Tata, M.E. Mechanical behavior of Nd:YAG laser welded aluminum alloys. *Procedia Struct. Integr.* **2020**, *28*, 132–138. [CrossRef]
20. Guan, Y.; Sun, S.; Zhao, G.; Luan, Y. Influence of material properties on the laser-forming process of sheet metals. *J. Mater. Process. Technol.* **2005**, *167*, 124–131. [CrossRef]
21. Cook, F.; Jacobsen, V.; Celentano, D.; Ramos-Grez, J. Characterization of the absorptance of laser irradiated steel sheets. *J. Laser Appl.* **2015**, *27*, 032006. [CrossRef]
22. Jablonka, A.; Harste, K.; Schwerdtfeger, K. Thermomechanical properties of iron and iron-carbon alloys: Density and thermal contraction. *Steel Res.* **1991**, *62*, 24–33. [CrossRef]
23. Davey, W.P. Precision Measurements of the Lattice Constants of Twelve Common Metals. *Phys. Rev.* **1925**, *25*, 753–761. [CrossRef]
24. Gražulis, S.; Daškevič, A.; Merkys, A.; Chateigner, D.; Lutterotti, L.; Quirós, M.; Serebryanaya, N.R.; Moeck, P.; Downs, R.T.; Le Bail, A. Crystallography Open Database (COD): An open-access collection of crystal structures and platform for world-wide collaboration. *Nucleic Acids Res.* **2011**, *40*, D420–D427. [CrossRef] [PubMed]
25. Hauk, V.; Behnken, H. *Structural and Residual Stress Analysis by Nondestructive Methods*; Elsevier: Amsterdam, The Netherlands, 1997; ISBN 444824766.
26. Sinha, M.; Karmakar, A.; Syed, B.; Ghosh, S. Effect of Austenite Conditioning on Martensitic Transformation in Commercial Grade Interstitial-Free Steel. *Met. Mater. Trans. A* **2020**, *51*, 3435–3446. [CrossRef]
27. Suarez, S.; Ramos-Moore, E.; Mücklich, F. A high temperature X-ray diffraction study of the influence of MWCNTs on the thermal expansion of MWCNT/Ni composites. *Carbon* **2013**, *51*, 404–409. [CrossRef]
28. Suarez, S.; Ramos-Moore, E.; Lechthaler, B.; Mücklich, F. Grain growth analysis of multiwalled carbon nanotube-reinforced bulk Ni composites. *Carbon* **2014**, *70*, 173–178. [CrossRef]
29. Rollett, A.; Humphreys, F.; Rohrer, G.S.; Hatherly, M. *Recrystallization and Related Annealing Phenomena*, 2nd ed.; Elsevier: Amsterdam, The Netherlands, 2004; ISBN 9780080441641.